Combustion and Flame 205 (2019) 135–146

Contents lists available at ScienceDirect

Combustion and Flame

journal homepage: www.elsevier.com/locate/combustflame

Buoyancy effect in sooting laminar premixed ethylene flame

Warumporn Pejpichestakul[a,b], Alberto Cuoci[a], Alessio Frassoldati[a], Matteo Pelucchi[a], Alessandro Parente[b,c], Tiziano Faravelli[a,*]

[a] CRECK Modeling Lab, Department of Chemistry, Materials and Chemical Engineering "G. Natta", Politecnico di Milano, Piazza Leonardo da Vinci 32, Milano 20133, Italy
[b] Ecole polytechnique de Bruxelles, Aero-Thermo-Mechanics Laboratory, Université Libre de Bruxelles, Avenue Franklin D. Roosevelt 50, CP 165/41, Brussels 1050, Belgium
[c] Combustion and Robust Optimization Group (BURN), Université Libre de Bruxelles and Vrije Universiteit Brussel, Brussels 1050, Belgium

ARTICLE INFO

Article history:
Received 9 January 2019
Revised 28 March 2019
Accepted 1 April 2019

Keywords:
PAH
Soot
Buoyancy effect
Laminar premixed flame
Kinetic modeling

ABSTRACT

Polycyclic aromatic hydrocarbons (PAHs) are known as soot precursors, but their formation/consumption is not fully understood. A recent comprehensive experimental study of premixed laminar ethylene flame [23] investigated the transition from gas-phase to soot particles. The complex fluid dynamics of this system is taken into account to compare model predictions with experimental measurements and thus further validate a detailed kinetic mechanism of soot formation. The relatively low inlet velocity and the large distance between the burner and the stagnation plate lead to significant influence of buoyancy, which requires a 2-D simulation. The observed constricted (necking) flame structure can be reproduced only using a comprehensive 2-D simulation, which includes buoyancy effects, radiative heat losses, and thermal diffusion. Predicted axial gaseous and PAH species profiles obtained from the CRECK mechanism are in good agreement with the measurements, especially even-carbon-number aromatics. Reasonable agreement of the predicted soot volume fraction profiles is also observed. Additionally, simulation results from different literature kinetic mechanisms are also discussed to highlight similarities and differences. The largest discrepancies among the predictions of the mechanisms are observed for phenylacetylene, a key-species representing the first building block of PAHs synthesis in flames.

A comprehensive analysis of relevant physical sub-models is also carried out in 2-D simulations. Additionally, predicted profiles from 2-D and 1-D simulations are compared. Following the literature, a 1-D simulation with imposed mass flux from the 2-D model was carried out to account for buoyancy effects. This approach provides an axial predicted flame temperature profile similar to the 2-D case. However, the predicted mole fraction profiles are quite different, especially for hydrogen and aromatics species because of the failure in accounting for the interplay of enhanced diffusion due to Soret effect, flame stretch, and large radial velocities in the proximity of the stagnation plane.

1. Introduction

Soot is well-known for its negative effects on health and environment, as well as on the efficiency of practical combustors. There have been many efforts in understanding the evolution of nanoparticle formation, particularly, in ethylene flames [1–7]. The soot modelers face numerous challenges, which can be divided in two main categories. The first aspect is the accurate prediction of gaseous and aromatic species that leads to the inception of soot particles. The other is the growth and oxidation of particles [8]. However, these challenges are inseparable as the growth of particles also relies on the accurate prediction of gaseous and aromatic species. In fact, without reliable gaseous and PAH predictions, it is not possible to study the missing pathways in soot formation, i.e. resonance-stabilized chain radical route [9,10]. Moreover, as better discussed in the following, soot particles largely affect flame temperature as a consequence of enhanced radiation.

Combustion diagnostics have been continuously advancing in terms of chemical species identification and quantification, thus providing useful information for detailed kinetic mechanism development and validation [11]. Recent experimental studies on PAH using optical diagnostics were mostly performed at low-pressure conditions [12–15]. These advanced techniques provide detailed information allowing the more in-depth understanding of fuel-specific chemistry [16]. There are several measurements of sooting premixed flames at atmospheric conditions, in which gaseous species up to PAHs [17–19] were measured. Dating back

* Corresponding author.
E-mail address: tiziano.faravelli@polimi.it (T. Faravelli).

https://doi.org/10.1016/j.combustflame.2019.04.001

approximately 20 years, several experimental measurements in sooting premixed flames were performed comprehensively, from small gaseous and aromatic species to soot quantifications [20,21]. This comprehensive experimental dataset represents an extremely valuable benchmark for the validation of detailed kinetic mechanism as the accuracy of soot kinetic models strongly relies on the accurate predictions of PAHs.

The International Sooting Flame (ISF) Workshop [22] aims at advancing the understanding of the phenomena involved in soot formation and oxidation in both laminar and turbulent regimes. It provides a useful database for soot mechanism development and to better understand soot evolution, in particular, for ethylene flames. However, the available data is usually limited to soot particles. Recently, Carbone et al. [23] carried out a comprehensive study covering the entire gas-to-particle transition in a single flame with similar operating conditions to the target ISF Premixed Flames 1 [22,24,25]. This new dataset is very valuable as it allows a comprehensive assessment of detailed kinetic mechanisms for gas-to-particles predictions. However, it has to be considered that this flame has a low inlet velocity and that the stabilization plate is placed at a large distance from the burner, leading to significant influence of buoyancy.

Xu et al. [26] experimentally investigated a sooting premixed ethylene/air flame at atmospheric conditions. Their study included streamwise velocity measurements along the flame. A rapid increase of velocity was observed in the post-flame region, which confirmed the significant effects of buoyancy. Buoyancy effects were treated using a 1-D simulation with imposed measured temperature and velocity profiles. Xuan and Blanquart [27] investigated the effect of two-dimensional geometry on soot formation, in the target flames from the ISF Workshop [22]. Their numerical study highlighted a flow entrainment and acceleration in all flames, which resulted in a variation of the mass flowrate along the flame centerline, impossible to capture with a traditional 1-D simulation. A modified 1-D simulation was proposed in [27], which essentially includes the two-dimensional effects by means of an imposed mass flowrate obtained from 2-D simulations, while retaining the solution of the energy equation. The predicted soot volume fraction profile using this modified 1-D approach showed good agreement with the corresponding 2-D predictions. However, the comparison of species profiles obtained from the modified 1-D simulations was not included in the above study.

The present work aims at studying PAH and soot formation in a laminar premixed ethylene flame, where buoyancy acceleration induces two-dimensional effects on the gas phase composition. The numerical results are compared with recent experimental data by Carbone et al. [23]. Moreover, the numerical results obtained from two-dimensional simulations are compared to modified 1-D computations.

The paper is organized as follows. The experimental configuration of the selected flame is described along with the computational mesh in Section 2. Numerical methods and the detailed kinetic mechanism used in this work are presented in Section 3. Model predictions and kinetic analyses, as well as, comparison with 1-D simulations are presented in Section 4.

Additionally, model predictions and kinetic analyses from different well-known PAH kinetic mechanisms in the literature are compared and discussed in Section S.1 of the Supplementary Material. Section S.2 discusses relevant physical properties and the appropriateness of different modeling approaches, i.e., buoyancy effect (S.2.1), radiative heat losses (S.2.2) and thermal diffusion (S.2.3).

2. Validation data set

The burner-stabilized premixed flame by Carbone et al. [23] is one of the few to include gaseous and PAH species together with soot particles in a single study. Namely, it investigates an atmospheric premixed flame of ethylene/air with a fuel-to-air ratio of 0.69, corresponding to an equivalent ratio (ϕ) of 2.07, and an average inlet velocity of 5.87 cm/s at standard temperature and pressure. The experimental device consists of a stainless steel honeycomb burner with an outer diameter of 4.8 cm. The shroud nitrogen flows constantly with a velocity of 0.21 m/s at 300 K through an outer annular region of the same honeycomb, with an outer diameter of 7.6 cm, to isolate the flame from external disturbances. A stagnation plate (diameter of 15 cm and thickness of 1.6 mm) is placed 4 cm above the burner to stabilize the flame. The temperature measured at the stagnation plate is 900 $\pm$ 50 K [23]. Temperature measurements were performed by a silica-coated R-type thermocouple with a spherical junction, and a rapid insertion technique. Temperature corrections were performed using a radiative–convective energy balance considering heat transfer of a sphere in a uniform flow.

Gaseous species were sampled using a fused silica capillary microprobe, which was radially inserted into the flame under vacuum. The sample is stored at 423 K to prevent condensation of heavy species. The sample is then injected to a gas chromatography/mass spectrometer system to quantify the concentration of hydrocarbons up to fluorene. The uncertainty of concentration measurements was estimated to be $\pm$7.5% for light hydrocarbons (up to C_2) and $\pm$15% for the heavier species [23].

3. Numerical simulation methods and kinetic mechanism

3.1. Kinetic mechanism

The high temperature gas-phase CRECK mechanism describes the pyrolysis and oxidation of a wide range of hydrocarbon fuels and includes the formation of PAHs up to pyrene. It adopts the C_0–C_2 core mechanism from Metcalfe et al. [28], C_3 subset from Burke et al. [29] and heavier components from Ranzi et al. [30]. The detailed mechanism describing combustion and PAH formation consists of 244 species and roughly 6000 reactions. The thermochemical properties were obtained from ATcT [31] and Burcat's databases [32]. The group additivity method [33,34] was used to estimate the thermochemical properties of unavailable species in the aforementioned databases.

A soot sectional model is adopted to follow the evolution from gaseous intermediates to particles. It discretizes the continuous size spectrum into a finite number of particles, represented by lumped pseudo species called BINs. The spacing factor between each size spectrum is fixed at 2. Lumped pseudo species (or BINs) are further discretized into different hydrogen content, denoted by descending order from A to C, to account for the fuel effect (different H/C ratio in the fuel) and the aging of soot particles, gradually assuming a graphitic-like structure. The soot model consists of 25 sections and three hydrogenation levels for stable molecules and radicals, leading to a total of 150 lumped pseudo species. The first four BINs (BIN_1–BIN_4) are heavy gas-phase PAHs. Soot particles start from BIN_5 with a diameter of approximately 2 nm. BIN_{12} are considered as a primary particle with a diameter of about 10 nm. Therefore, BIN_5–BIN_{12} are considered spherical particles. The particles larger than BIN_{12} (BIN_{13}–BIN_{25}) are aggregates with a constant fractal dimension of 1.8. Reactions involving heavy PAHs determine the particle inception, accounting for sticking probability, whose value depends on the size of colliding entities and the temperature, as estimated from the comparison with molecular dynamics simulations [35,36]. The coagulation and aggregation of particles occur through reactions involving soot particles and aggregates. The reference rate of inception and coagulation rate (k) depends on the temperature- and size-dependent collision efficiency (γ), and the collision frequency evaluated using the

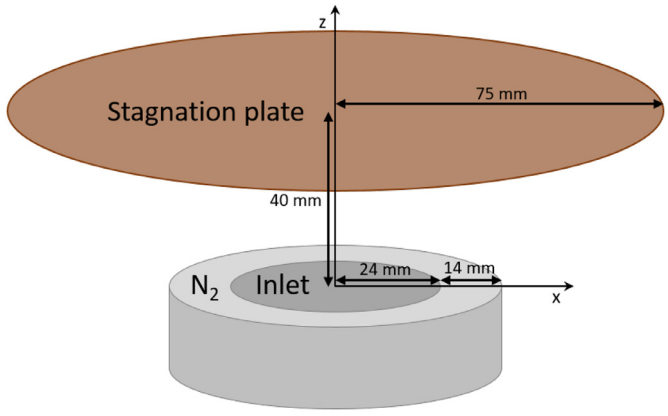

(a) Schematic of the burner.

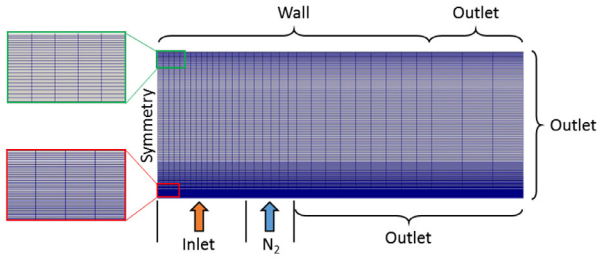

(b) Computational mesh

Fig. 1. Schematic of the burner and computational mesh.

number of carbon atom (nC): $k = \gamma 1.6 \times 10^{13} T^{0.5} nC^{1/6}$ cm^3/mol/s [37]. Other reactions, i.e., surface growth by acetylene addition, gaseous species and PAH condensation, dehydrogenation, H-abstraction and oxidation, are discussed elsewhere [38].

The soot sub-mechanism is coupled to a high temperature gas-phase mechanism. The overall kinetic mechanism consists of approximately 400 species and over 25,000 reactions. The complete soot mechanism used in this work (CRECK1800s) has been extensively validated against laminar premixed flames of different fuels in a wide range of operating conditions as discussed elsewhere [39] and is attached in the supplemental material together with thermodynamic and transport properties.

3.2. Numerical methods

The laminar premixed flame simulations presented in this work were carried out with the detailed kinetic mechanism using 2-D and 1-D simulations. 2-D simulations were performed using the laminarSMOKE code [40], which adopts the open-source OpenFOAM platform. 1-D simulations were performed using the OpenSMOKE++ code [41].

3.2.1. 2-D model

Figure 1(a) presents a two-dimensional scheme of the computational domain investigated in the numerical simulations. The temperature of unburnt gas is 323 K [23]. Figure 1(b) shows the computational mesh used in the simulations. It is an axisymmetric, structured, non-uniform mesh containing ~8000 cells, sufficient to ensure grid insensitive results.

The laminarSMOKE code [40] is a numerical solver based on the operator-splitting algorithm designed to manage very detailed kinetic mechanisms. Reactive and laminar flows are solved in multi-dimensional geometries using the finite volume method. The conservation equations of mass, momentum, species and energy are solved by assuming a Newtonian fluid. The transport terms, i.e., convection and diffusion, are solved using the backward (or implicit) Euler's method. The stiff ODE system of chemical reactions is solved using the OpenSMOKE++ ODE solver [41]. The PISO algorithm is applied to ensure the conservation of mass at each time step. The diffusion velocity includes Fickian and thermal diffusion. Radiative heat losses from gaseous-species and soot particles is accounted using optically thin approximation [42,43]. The transport properties are calculated on the basis of the kinetic theory of gases using the same implementation approach adopted in CHEMKIN [44]. The relevant transport parameters (Lennard-Jones (LJ) coefficient, polarizability, etc.) for individual chemical compound are provided as input using the CHEMKIN format. A thermophoretic coefficient of 0.538 is used in present work, which was discussed in [45]. The studies of thermophoretic effect are also discussed in detail elsewhere [46,47].

In order to reduce the numerical issues associated with the complexity of the complete mechanism (~400 species and ~25,000 reactions), a first guess solution is obtained using a skeletal mechanism (25 species and 155 reactions). Once the first guess is available, the detailed mechanism without soot is adopted to refine the solution. Finally, the complete mechanism, including soot, is used to attain the final solution. The CFD code is fully parallel, based on the decomposition domain technique, which consists in dividing the mesh in a number of sub-meshes equal to the number of available processors. Formally, both the transport and the chemical steps are accelerated. The 2-D simulations with the complete mechanism, including soot, require over 60,000 CPU-hours utilizing 80 Intel Xeon processors to ensure convergence.

3.2.2. 1-D model

The 1-D simulations are carried out using OpenSMOKE++ suite by Cuoci et al. [41]. It includes several 1-D simulation solvers which are burner-stabilized, burner-stabilized stagnation, and counterflow configurations for both premixed and diffusion flames. The performed simulations solve the energy equation and also account for radiative heat losses using optically thin approximation and the effect of soot on flame radiation. Diffusion velocities of small gaseous species and soot particle are considered according to the same approach described in Section 3.2.1. To ensure the smoothness of calculated profiles, gradient and curvature coefficients of the solutions are set to 0.05 and 0.5, respectively, which lead to a total grid point of ~300. For the modified 1-D simulations, based on the imposed mass flux [27], the convective velocity is not solved. The 1-D simulations with the imposed mass flux, which serially work, require ~20 CPU-hours to ensure convergence.

4. Results and discussions

The 2-D complete simulation, named AB (accounting for buoyancy), includes the buoyancy effect, radiative heat losses from gaseous and soot emissivities [42,43], and accounts for thermal diffusions from small gaseous species (Soret effect) and soot particles (thermophoretic effect). The model predictions from the CRECK kinetic mechanism are compared with the experimental data, for major species, PAHs, and soot volume fraction. The mechanism implications are analyzed and discussed with particular attention to the formation of aromatic species and soot precursors. As already demonstrated in a previous work [39], an important effect of soot formation and growth on intermediate PAHs predictions is observed also in this flame. The 2-D complete (AB) simulations, accounting for all effects, are also compared with simulation results obtained from 1-D models.

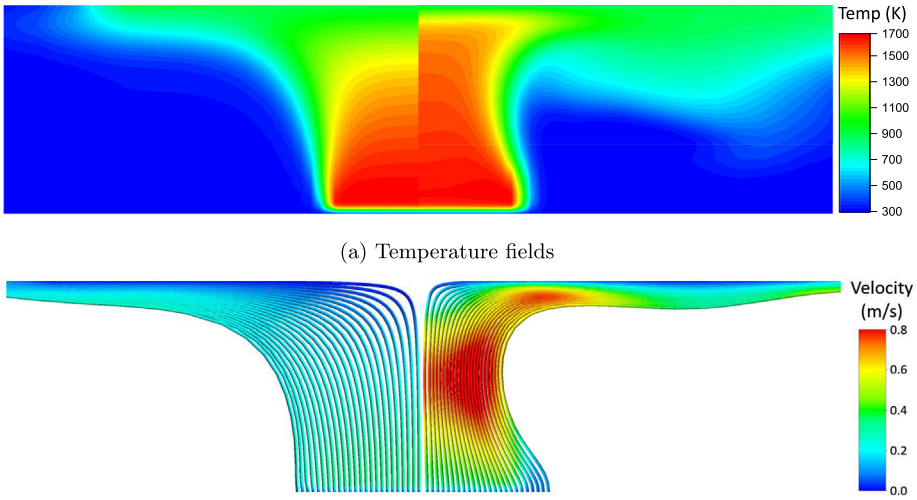

(a) Temperature fields

(b) Stream lines

Fig. 2. Comparison of temperature field and stream lines calculated from the "complete" model (right) and the model neglecting buoyancy effect (left).

4.1. Flame structures and major species predictions

First, it is important to assess the flame structure and the flow field in order to investigate several effects associated to numerical simulations. Figure 2 shows the buoyancy effect on the temperature map and stream lines. The predicted temperature field (right panel of Fig. 2(a)) shows that the "complete" model is able to reproduce the constricted flame structure as observed experimentally (see [23]). The buoyancy effect is the consequence of the low inlet velocity and long distance between the burner and the stagnation plate. Thus, the Froude number (Fr) of this flame is lower than 1. The streamlines (Fig. 2(b)) clearly highlight the deflection of the flame caused by buoyancy-driven forces. The strong density gradient between the flame and post-flame region further induces the reduction of pressure due to buoyancy ($p = p_0 + \rho gh$). This also causes pressure differences with the environment, which lead to the radial contraction of the flow streams. These synergistic behaviors result in the acceleration of the axial velocity.

In order to quantitatively compare the model predictions with the experiments, Fig. 3(a) shows the measured and calculated axial temperature profiles. The model successfully predicts the flame region, which is located at $\sim$0.2 cm from the burner. The buoyancy effect, which accelerates the burnt gases, explains the higher predicted temperature in the post-flame zone ($>$0.5 cm) in comparison to neglecting buoyancy (see Section S.2.1), which agrees with the experimental data. The dotted line is the 3-D simulations computed by Carbone et al. [23], with the flame conditions obtained from a preliminary equilibrium computation for the post-flame products, without solving chemistry and neglecting thermal diffusion. The prescribed flame conditions included the maximum flame temperature of 1680 K with uniform axial velocity of 0.33 cm/s and concentrations of major species (N_2, CO_2, CO, C_2H_4, O_2, OH•, H•).

The results from the CRECK mechanism (black lines) slightly under-predict the flame temperature by $\sim$60 K, which is within the experimental uncertainties as the measured temperature was corrected due to radiative heat losses as high as $\sim$110 K [23]. The same under-prediction of the flame temperature is also observed with other kinetic mechanisms, as discussed in Section S.1.

The effect of soot particles emitting radiative heat is also evident (dashed lines). Figure 3(b) compares the axial temperature profiles between the measurements and model predictions, where predicted temperature profiles are shifted by 60 K to match the maximum measured temperature. This allows to better

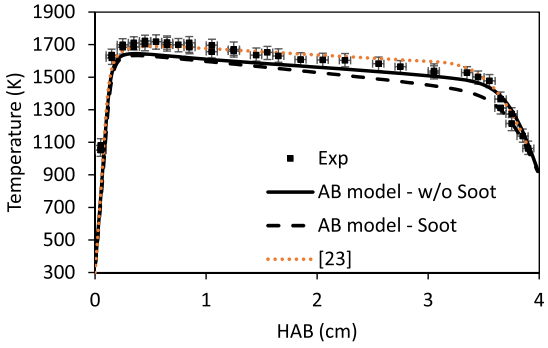

(a) Temperature profile without shift

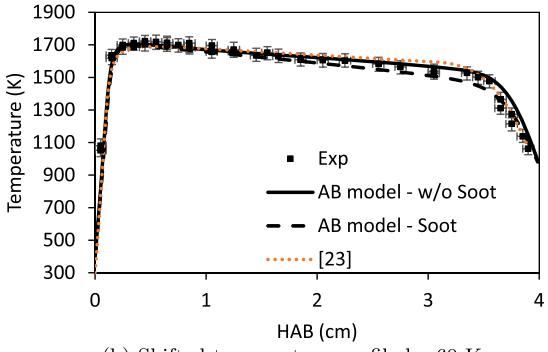

(b) Shifted temperature profile by 60 K

Fig. 3. Comparison of measured (symbol) temperature profiles and results from simulation using CRECK mechanisms (black lines) and 3-D simulation from Carbone et al. [23] with frozen chemistry. Solid line: effect of neglecting the soot sub-mechanism. Dashed line: effect of including the soot sub-mechanism. Dotted lines: 3-D simulation from [23].

qualitatively investigate the decay of temperature resulting from soot radiation effects in the post-flame region. It is worth mentioning that the temperature shift here applied is not strictly related to the experimental uncertainty. The inclusion of the soot sub-mechanism does not affect the predicted maximum flame temperature, but reduces the post-flame temperature up to $\sim$80 K. In fact, both predicted profiles can capture the measured profile quite well, but the model accounting for soot radiative heat losses results in a better agreement in the region close to the stagnation plate.

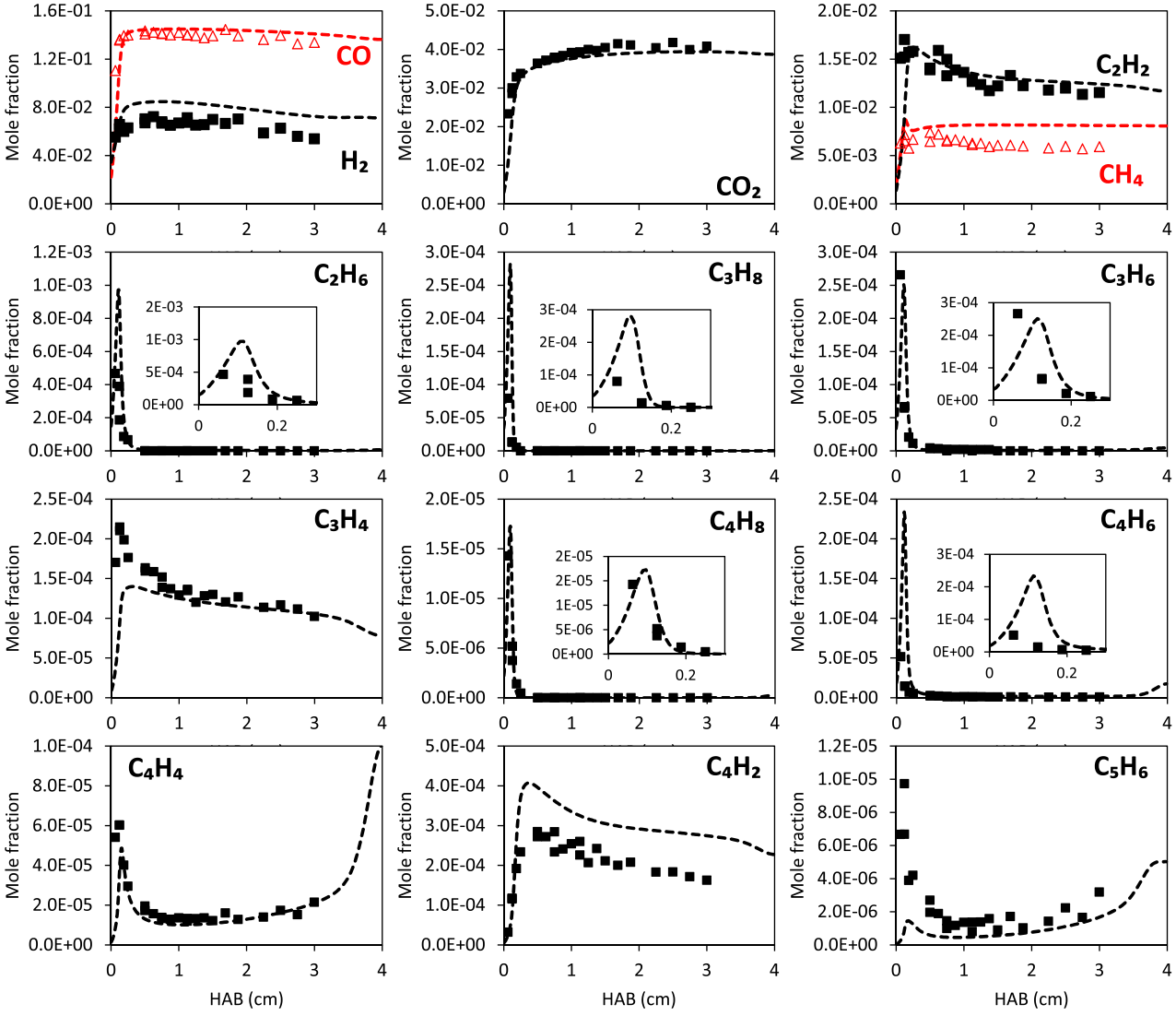

Fig. 4. Mole fraction profiles of small gaseous species between the measurement (symbols) and the model predictions using the CRECK soot mechanism (lines).

Figure 4 compares experimental profiles of small gaseous species with predictions from the CRECK mechanism [39]. The model captures the CO profile quite well. The predicted CO_2 also agrees with the measurements, which implies that the mechanism properly characterizes the fuel combustion and flame temperature. The model slightly over-predicts H_2 concentration, highlighting an overly pronounced role of H-abstraction reactions by H•, as shown in Fig. 5(a). Radial diffusion is responsible for the observed H_2 decrease in the post-flame zone and this effect is well captured by the model. The prediction of acetylene (C_2H_2), a key component in molecular weight growth, is also quite satisfactory. Acetylene is generated in the flame and is consumed in the post-flame region through the formation of propargyl radical (C_3H_3•) and aromatic species via acetylene addition. The measured C_3H_4 profile is the sum of allene (C_3H_4-A) and propyne (C_3H_4-P). C_3H_4 is formed in the flame region through the recombination of H• with propargyl radical. The model under-predicts the maximum concentration of C_3H_4, but it captures the downstream consumption quite well.

Some discrepancies are observed in the predictions of diacetylene (C_4H_2), butadiene (C_4H_6) and cyclopentadiene (C_5H_6). Despite a slight over-prediction, the predictions of stable polyyne species (i.e. diacetylene, C_4H_4) qualitatively well agrees with the experimental data. A 3-fold over-prediction of 1,3-butadiene (C_4H_6) is observed suggesting the need of further investigating its pyrolytic and oxidative chemistry. Zhou et al. [48] recently suggested that C_4H_6 oxidation can lead to allene formation. Therefore, also C_3H_4 predictions could benefit from a better assessment of C_4H_6 kinetics.

Figure 5(b) shows the rate of production analysis (ROPA) of cyclopentadiene along the centerline of the flame. Despite its low concentration in these conditions, the under-prediction of the peak concentration of cyclopentadiene deserves a specific discussion. This under-prediction is mainly related to H-abstraction by H• [49], also contributing to an over-prediction of H_2.

Overall, the model is able to capture all small gaseous species reasonably well with some discrepancies for some minor species. It should be noted that this complex flame is not the most adequate set-up to assess relevant reaction kinetics. Specific analysis about C_3H_4 and C_4H_6 and C_5H_6 will be further investigated using these components as reactants, allowing a better understanding of their primary reactions.

4.2. Aromatic predictions and soot effect on intermediate aromatics

Aromatic formation is clearly favored at rich conditions. Figure 6 shows the comparison of experimental profiles of aromatic species model predictions (dashed lines). A more detailed discussion regarding the effect of neglecting the soot

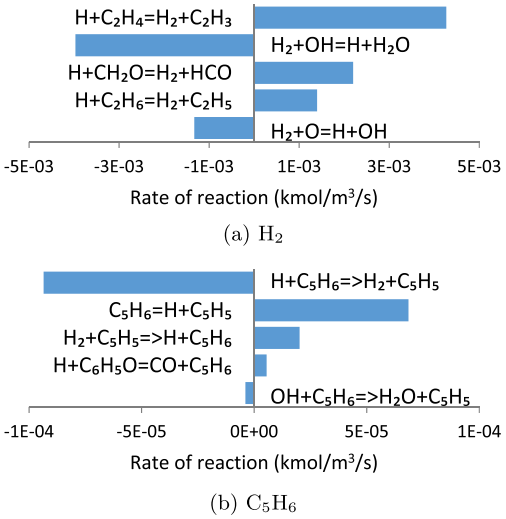

Fig. 5. Global rate of production analysis of small gaseous species.

sub-mechanism on PAH predictions (solid lines) is provided at the end of this section. The measurements clearly show the fuel dependency in aromatic formation, i.e., the different concentration between even- and odd-carbon-atom aromatic species, due to the lower concentration of CH_4 in comparison to C_2H_2 in an ethylene flame. Experimental data of even-carbon-atom aromatics (benzene, phenylacetylene, naphthalene and acenaphthylene) on the left side of Fig. 6 are in the range of approximately 10–100 ppm, which is higher than the range of odd-carbon-atom species. The relatively low concentration of CH_3• leads to a much lower amount of toluene (C_7H_8) compared to benzene. Namely, about 2 orders of magnitude difference is observed between benzene and toluene. As observed experimentally, the mass yield of benzene (C_6H_6) is comparable to that of C_3H_4. Most of the aromatic species start forming in the flame and progressively grow in the post-flame region with the exception of toluene. Moreover, a plateau can be experimentally observed for some of these even-carbon-atom aromatics species in the post-flame region highlighting the competing role of formation and consumption channels as further discussed below.

In general, the simulation results provide reasonable agreement with the experimental data. Modeled benzene profiles, mostly determined by C_3H_3• recombination reaction, well agrees with the measurements. The model predictions of larger even-carbon-atom aromatic species are quite satisfactory too. In order to visually assess the qualitative agreement, Fig. 7 compares experimental and calculated mole fraction profiles of phenylacetylene ($C_6H_5C_2H$), respectively plotted on two different axes. Although the model overpredicts phenylacetylene by a factor of 4, it provides good qualitative agreement, in particular in terms of a correct characterization of the plateau behavior occurring at HAB $>$ 0.8 cm. This plateauing behavior associates to soot formation. Figure 8 shows the formation rate (net rate between production and destruction rates) of phenylacetylene in comparison with its condensation rate on soot particles. The comparison between formation rate and mole fraction profile shows that phenylacetylene initially forms just after the flame location and drastically increases via HACA mechanism. At the post-flame region, the condensation of phenylacetylene on soot particle starts at HAB $\sim$ 0.5 cm, where the incipient particles form. These soot growth reactions counterbalance phenylacetylene formation downstream of the flame region, resulting in the plateau profile.

Model predictions of larger PAH quantitatively agree with the measurements. Figure 9 shows the pathway of even-carbon-atom PAH formation. As expected, the HACA mechanism plays the most important role. The contributions of acetylene addition to each PAH are quite similar (i.e. same order of magnitude, 10^{-5} kg/m^2/s). The first successive addition of acetylene on phenyl radical (C_6H_5•) favors phenylacetylene rather than $C_6H_5C_2H_2$. This selectivity is consistent with the theoretical calculations by Mebel et al. [50].

In summary, the CRECK mechanism provides reasonable agreement for naphthalene and acenaphthylene. Even considering the soot formation, an over-prediction of benzene by $\sim$40% is observed. The largest discrepancy is associated to the formation of phenylacetylene, which is over-estimated by a factor of $\sim$4. Although the experimental study [23] estimated experimental uncertainties of $\sim$15% for species larger than C_2, it is worth noting that the concentration measurements were carried out using an intrusive technique, which may induce some perturbations. However, this large error in phenylacetylene yields is also observed adopting other detailed kinetic mechanisms (see Section S.1). It is difficult to explain such a deviation as the major precursor of phenylacetylene (benzene) and the successive products of the even-carbon-atom PAH growth (naphthalene and acenaphthylene) are both predicted with acceptable accuracy.

Soot effect on intermediate PAHs has been discussed in detail elsewhere [39], taking into consideration a large number of flames and a wide range of conditions. The previous Fig. 6 also shows the effect of neglecting the soot sub-mechanism on aromatic profiles (solid lines). When neglecting soot formation, the agreement with the experimental data of major aromatic species worsens with an average increase of the concentrations by $\sim$30–40%. The improvement obtained by the complete mechanism is both quantitative and qualitative, in particular, for the characterization of the plateau behaviors which are experimentally observed in the post-flame region. The inclusion of the soot sub-mechanism affects the minor aromatic species, i.e., toluene and indene (C_9H_8) in a peculiar way. Indene is formed from different pathways, i.e., acetylene addition on benzyl radical, propargyl addition on phenyl radical, and oxidation of oxygenated naphthalene (naphthoxy/naphthol). Trace amounts of methyl-naphthalene and fluorene are observed in the measurement. The less satisfactory prediction can either come from their over-consumption in the soot sub-mechanism, or the underprediction of their formation rates. Further theoretical and experimental investigations of toluene and indene should be carried out in wider range of operating conditions. Similarly, further attentions should be devoted to the formation and consumption of trace amount species such as methylnaphthalene ($C_{10}H_7CH_3$) and fluorene ($C_{13}H_{10}$).

4.3. Soot prediction

Figure 10 shows the predicted soot volume fraction profile and the measurements obtained with different experimental techniques. Carbone et al. [23] performed soot volume fraction measurement using optical techniques, consisting of laser light extinction (LE) measurements with a wavelength of 633 nm and pyrometry measurement. Maricq [51] performed an experimental study at similar conditions, with an equivalence ratio of 2.06 and the same cold gas velocity, but the stabilization plate was placed at HAB = 2.3 cm. Soot measurements were carried out using differential mobility analysis (DMA). The soot volume profiles from DMA measurement are obtained from the integration of the soot size distribution functions presented by Carbone et al. [23].

The discrepancy between the different measurements highlights the difficulties related to soot measurements and the existing large experimental uncertainty, which needs to be considered when comparing predicted and measured soot profiles in flames. The modeled soot volume fraction was computed assuming a soot density of 1.5 g/cm^3, which is in line with the effective density observed by Camacho et al. [1] for incipient soot. The model

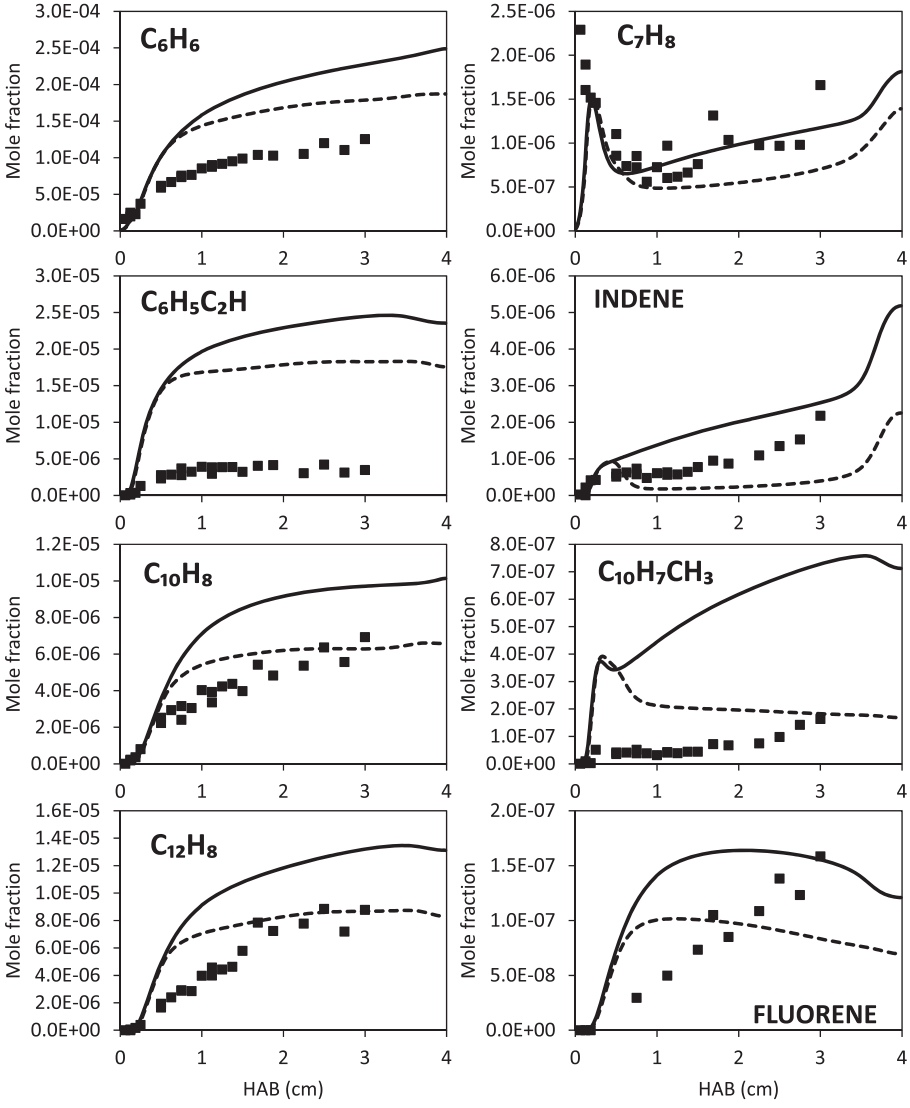

Fig. 6. Comparison between measured (symbols) and predicted (lines) mole fraction profiles of aromatic species. Solid lines: CRECK PAH mechanism. Dashed lines: CRECK PAH + soot mechanism.

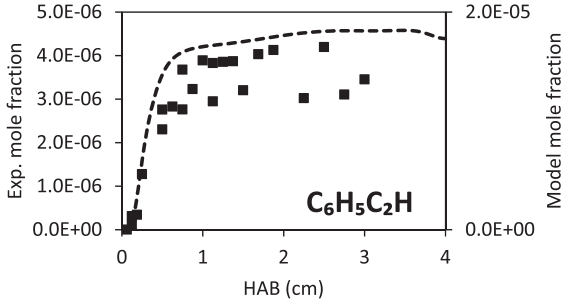

Fig. 7. Comparison between measured (symbols) and calculated (lines) mole fraction profiles of phenylacetylene.

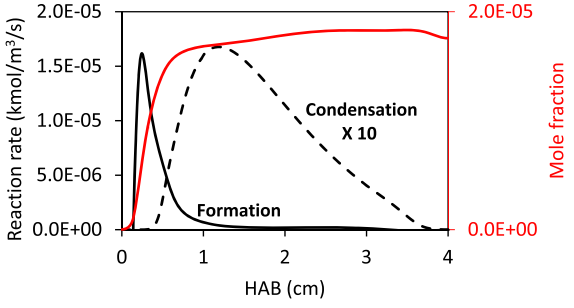

Fig. 8. Plateau analysis of phenylacetylene. Black solid line: formation rate. Black dashed line: rate of phenylacetylene condensation on soot particle. Red line: mole fraction profile. (For interpretation of the references to colour in this figure legend, the reader is referred to the web version of this article.)

predictions capture the incipient soot location at ~0.5 cm above the burner, which agrees with the experimental observations from laser light extinction (LE) and pyrometry measurements. Following soot nucleation, the model predicts a sharper increase of soot volume fraction, which subsequently leads to an over-prediction by approximately a factor of ~4. This discrepancy between the model predictions and measurements could suggest that surface growth reactions could be overestimated. The soot sub-mechanism includes surface growth reactions from different growth and condensed species, i.e., C_2H_2, resonantly-stabilized radicals and PAHs. However, the comparison of the different experimental profiles in Fig. 10 clearly shows a quite large uncertainty range associated to soot volume fraction measurements.

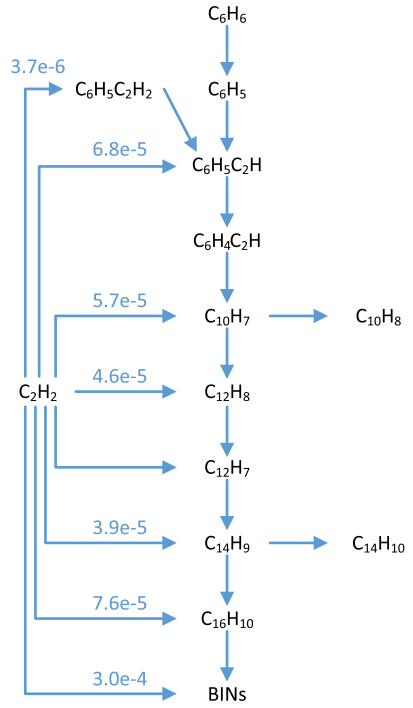

Fig. 9. Reaction pathway analysis of PAH formation and flux of acetylene addition ($kg/m^3/s$) at HAB = 1 cm.

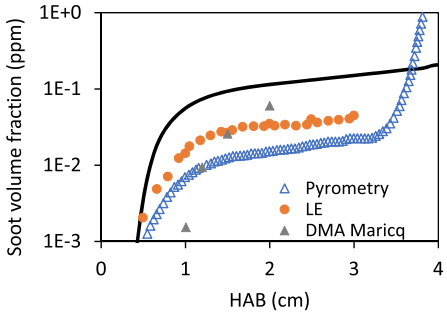

Fig. 10. Comparison between measured soot volume fraction profile according to different techniques (symbols) and model predictions (line). Triangles: pyrometry measurements [23]. Circles: laser light extinction (LE). Diamonds: differential mobility analysis (DMA) by Maricq [51].

4.4. Comparison between 2-D buoyancy model and modified 1-D simulations

The 2-D simulations are computationally demanding, in particular with large detailed mechanisms. Thus, some strategies have been proposed in the literature to simplify these complex phenomena using quasi 1-D simulations, such as opposed-flame solver [52] and 1-D simulation with the imposed mass flux derived from 2-D simulation [27]. This section compares the calculated results obtained from the complete 2-D simulation with these different simplified 1-D numerical approaches. In order to compare the prediction of soot volume fraction profiles, the simulations are carried out using the CRECK mechanism coupled with soot submechanism.

Before comparing the speciation predictions, it is important to analyze the predicted flame structure with 1-D simulations. Figure 11 compares the measured and predicted axial temperature profiles. As discussed in Section S.2.2, radiative heat losses play a major role, and cannot be neglected. Accounting for radiation in 1-D opposed flame simulations lead to strong temperature

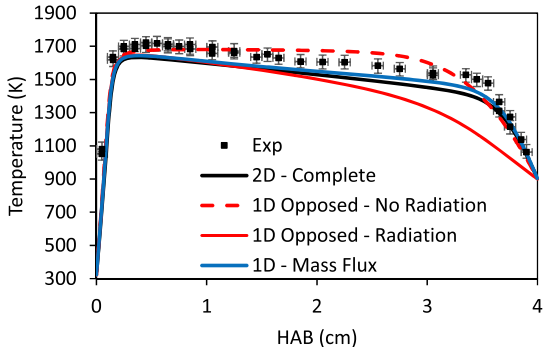

Fig. 11. Comparison between measured (symbols) and predicted (lines, CRECK model) temperature profiles. Black lines: 2-D simulations. Red lines: 1-D simulations using opposed flame solver. Blue line: 1-D simulating with imposed mass flux from 2-D. (For interpretation of the references to colour in this figure legend, the reader is referred to the web version of this article.)

under-predictions, because of the absence of buoyancy effect. On the other hand, neglecting radiation provides slightly better predictions, showing only a small over-prediction of post-flame temperatures. The calculated flame structure obtained from the standard 1-D opposed flame solver with the exclusion of radiative heat losses may mislead the validation due to the error compensation between buoyancy-driven force and radiative heat losses. Therefore, the obtained flow field from the standard 1-D opposed flame solver is not appropriate to validate chemistry evolution.

On the contrary, the modified 1-D solver with the imposed mass flux suggested by Xuan and Blanquart [27] (blue line) can predict similar temperature profile as the 2-D model. This modified 1-D model solves energy equation with the radiative heat losses from gas and soot radiation as in the 2-D model. A small discrepancy is observed near the plate, where the over-prediction is ~30 K. Soret effect in the modified 1-D simulation does not play a role in the flame structure prediction.

Figure 12 shows the comparison of major species profiles between modified 1-D and 2-D simulations. The predictions of major species (CO, CO_2, CH_4 and C_2H_2) from modified 1-D simulations are similar to those of 2-D simulations, in terms of flame location. However, some differences can be observed in the post-flame region. The largest discrepancy between modified 1-D and 2-D simulations is the prediction of H_2 profiles. Predicted H_2 profile using 2-D simulation can capture the reduction along the centerline due to the radial convection/diffusion. In contrast, the modified 1-D simulations conserve the mass in the whole domain, leading to ~20% over-prediction of H_2. The inclusion of Soret effect in modified 1-D simulations (dashed lines) leads to the anomalous accumulation of H_2 near the stagnation plate. The predictions of other major species using the modified 1-D model are also affected by this radial effect.

The differences in H_2 predictions lead to relevant deviations in the PAH estimations. Figure 13 shows the comparison of aromatic profiles between the measurements and model predictions. As expected, the discrepancies between 1-D and 2-D simulations are mainly observed in the post-flame region, where the effects of buoyancy, flame stretch and radial diffusion play a major role. The modified 1-D results show a reduction in mole fraction profiles for all aromatic species, which leads to different trends and qualitatively disagree with the experimental data. The largest differences (20–30%) are observed for phenylacetylene and acenaphthylene profiles close to the stagnation plate. Accounting for Soret effect in modified 1-D simulation induces a strong reduction of PAHs concentration, corresponding to the over-prediction of H_2, particularly in the region close to the stagnation plate.

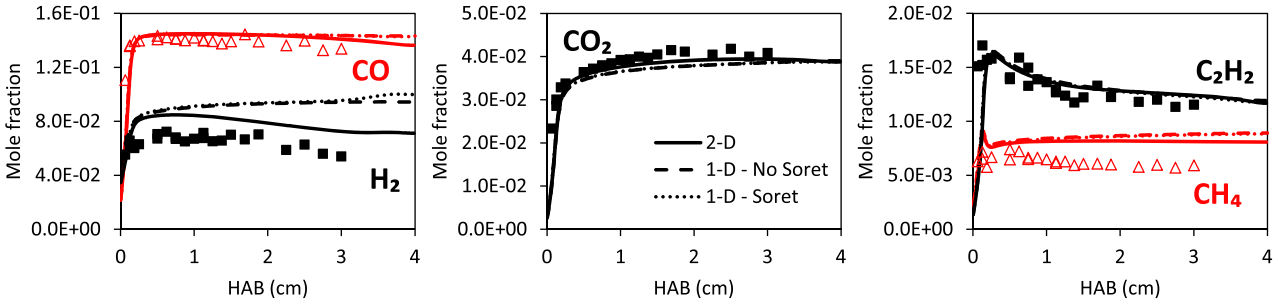

Fig. 12. Comparison of major species profiles. Measurements (symbols) and calculated profiles using the CRECK mechanism (lines). Solid lines: 2-D simulations. Dashed lines: imposed mass flux 1-D simulations without Soret effect. Dotted lines: imposed mass flux 1-D simulations with Soret effect.

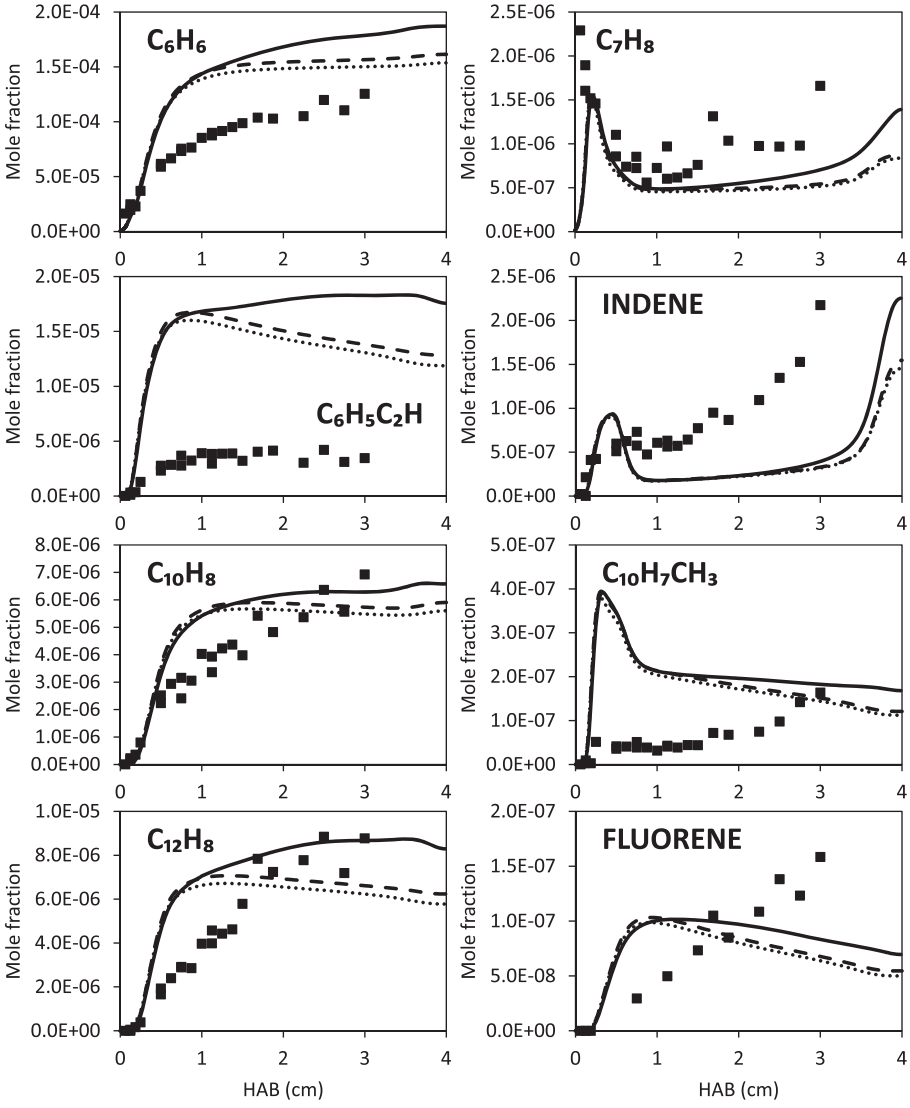

Fig. 13. Comparison of major species profiles. Measurements (symbols) and calculated profiles using the CRECK mechanism (lines). Solid lines: 2-D simulations. Dashed lines: imposed mass flux 1-D simulations without Soret effect. Dotted lines: imposed mass flux 1-D simulations with Soret effect.

Figure 14 shows the comparison between measured and predicted profiles of hydrogen and the sum of all the aromatics (panel (a)), and soot volume fraction (panel (b)). Figure 14(a) compares H_2 and aromatic profiles along the HAB. The predicted aromatic profiles are adjusted by a factor of 1.5 in order to better compare the qualitative agreement. The predicted aromatic profiles from 1-D simulations deviate from HAB $\sim$1 cm, while the predicted H_2 profiles differ downstream of the flame location. The discrepancies of aromatics concentration between 1-D and 2-D are roughly 20%, which is associated to the difference in H_2 predictions. Clearly, the impossibility of capturing the radial effect with 1-D simulations causes an accumulation of H_2 in the flame, which is reflected in both quantitative and qualitative discrepancies in aromatic predictions.

Figure 14(b) compares the predicted and measured soot volume fraction profiles. The modeled soot volume fraction from 1-D sim-

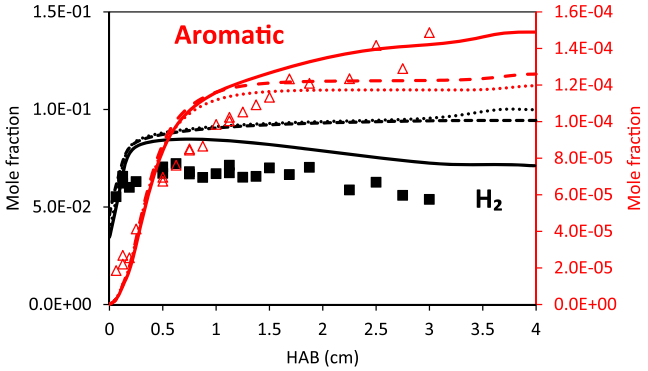

(a) Mole fraction profiles of H_2 and aromatics. Predicted aromatic profiles are adjusted by a factor of 1.5.

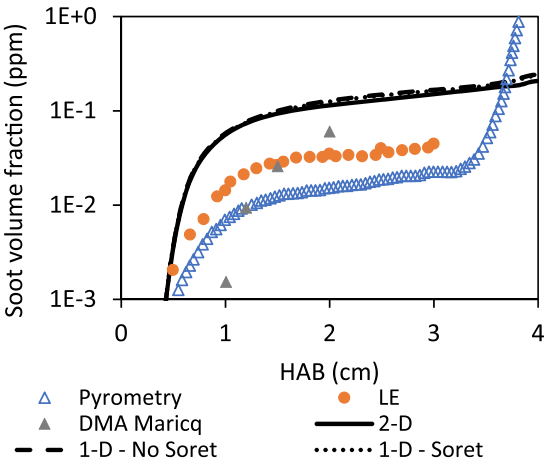

(b) Soot volume fraction profiles.

Fig. 14. Comparison of mole fraction and soot volume fraction profiles. Measurements (symbols) and calculated profiles using CRECK mechanism (lines). Solid lines: 2-D simulations. Dashed lines: imposed mass flux 1-D simulations without Soret effect. Dotted lines: imposed mass flux 1-D simulations with Soret effect.

ulation slightly differs at HAB $>$ 1 cm. Similar soot predictions from 2-D and 1-D models are observed, which agrees with the calculations by Xuan and Blanquart [27]. In fact, the comparison of soot volume fraction represents the mass yield of particles which is less influenced by H_2.

Although the predicted flame structure and soot volume fraction obtained from imposed mass flux 1-D simulations seem promising, the comparisons of species profiles suggest that the modified 1-D is not able to capture H_2 and PAHs in the flame and, especially, in the post-flame region, which further influences the prediction of other species such as PAHs. The buoyancy effect affects flow fields and temperature profiles in both radial and axial directions. The different flow field leads to large radial velocity differences and causes the flame stretch. The variation in radial velocity cannot be captured in 1-D simulations. The different radial temperature enhances the radial thermal diffusion of H_2 due to Soret effect that leads to different concentration fields as discussed in Section S.2.3. The imposed 1-D simulation neglects the radial diffusion and the variation in radial velocity associated to buoyancy. Modified 1-D simulation should be carried out with particular attention and avoiding, in particular, the validation of kinetic mechanisms through the comparison of model predictions with the experimental data in terms of mole fraction.

The buoyancy effect plays an important role, pointing at the need of 2-D simulations in order to validate the species concentration. The experimental study should minimize the buoyancy effect involved in the measurement through the preliminary Froude number calculation, allowing to choose an appropriate inlet velocity and distance between the stagnation plane and the burner. The solution could be either increasing the inlet velocity or decreasing the distance between the stagnation plate and the burner. However, as highlighted in [39], it is important to study the formation of PAHs and soot simultaneously. Therefore, the residence time should be sufficiently long, which constrains the experimental design. For premixed flames, the burner-stabilized stagnation flame [1] configuration, which is quite attractive for soot studies, can be modeled using quasi 1-D simulations, but unfortunately, gaseous species and PAH measurements are difficult to carry out. The configuration adopted by Carbone et al. [23], due to a larger distance of the stagnation plane, provides access to probes to measure gaseous species including PAHs. This is an important advantage, but the drawback is that a 1-D simulation cannot be adopted. However, the study presented in this paper shows that it is nowadays feasible to perform a 2-D simulation able to characterize simultaneously PAHs and soot formation.

5. Conclusion

A detailed kinetic mechanism is validated against the measurements of a comprehensive study of premixed laminar ethylene flames in sooting conditions by Carbone et al. [23] adopting a 2-D simulation. This complete 2-D model includes buoyancy, radiative heat losses, and thermal diffusion. 2-D simulations are carried out using the laminarSMOKE code [40] and its dedicated numerical tools able to handle stiff chemistry and large mechanisms.

This flame is characterized by the presence of a significant buoyancy, which leads to the constriction in the post-flame region that accelerates the burnt gas resulting in a higher flame temperature. Computed axial temperatures are compared with the experimental data, indicating an under-prediction of $\sim$60 K, which is close to the experimental uncertainty of the measurements considering the correction at most of 110 K. Predicted major gas-phase species concentration profiles along the centerline agree with the experimental data quite well (i.e. $<$15%). Model predictions of C_2–C_5 species are in reasonable agreement with the experimental measurements. The difference of predicted C_2H_2 concentration is $\sim$5%, while the predicted butadiene profiles show the largest deviation of about 3 times.

Predictions of single ring aromatics and PAHs are also in general good agreement with the experimental data, with discrepancies mostly within 50%. The model is able to predict the major aromatic species, especially even-carbon-atom PAHs, quite satisfactorily. The largest discrepancy is observed for phenylacetylene prediction, which is overestimated by a factor 4. The model is able to characterize the plateau behavior that is observed experimentally for some aromatics in the post-flame region because of a counterbalancing effect between their formation from gaseous species and their consumption due to soot growth. Soot effect on intermediate aromatic species concentration results in a reduction of $\sim$30–40%. The predicted soot volume fraction profiles reasonably agree with the measurement with an over-prediction of a factor of 4. However, the model can predict the inception of particle at HAB $\sim$0.5 cm, which is in good agreement with the experimental data. Comparisons of species profiles predictions from other literature PAH mechanisms are carried out using the complete 2-D simulations. Predicted flame structure and temperature are similar for all the mechanisms, except ABF mechanism (Appel et al. [53]) showing under-predictions as large as $\sim$200 K. Over-predictions of PAH are observed for most of the models, especially for phenylacetylene

which is over-predicted by over 1 order of magnitude by these kinetic models.

Effects of different physical processes are also investigated using the 2-D simulation model. Buoyancy effect plays a major role in the characterization of the flame structure. Neglecting buoyancy leads to an underestimation of axial velocity in the post-flame region, which results in the under-prediction of post-flame temperature. The lower downstream velocity and temperature lead to different flow history and residence times. Neglecting radiative heat losses increases post-flame temperature. Soret effect plays a role in the post-flame region near the plate because of the high temperature gradients.

Standard 1-D opposed flame solver accounting radiative heat losses is not able to reproduce flame structure as it lacks the buoyancy effects. Its predictions without radiative heat losses are in better agreement with temperature measurements but this is a misleading result due to the error compensation between absence of buoyancy and neglecting heat losses. Computed temperature profiles from modified 1-D simulations with an imposed mass flux are similar to the ones of the complete 2-D simulation. However, they cannot reproduce the radial diffusion/convection effect. In particular, 1-D simulation cannot capture the diffusion of hydrogen, thus producing large deviations in the predictions of PAHs. Thus, this flame, which provides a unique experimental dataset comprising major species, PAHs and soot, can only be simulated using a 2-D model.

Acknowledgments

The authors gratefully acknowledge Dr. Francesco Carbone and Prof. Alessandro Gomez from Yale University for providing the measurement profiles. This project has received funding from the European Union's Horizon 2020 research and innovation programme under the Marie Sklodowska-Curie grant agreement no. 643134.

Supplementary material

Supplementary material associated with this article can be found, in the online version, at doi:10.1016/j.combustflame.2019.04.001.

References

[1] J. Camacho, C. Liu, C. Gu, H. Lin, Z. Huang, Q. Tang, X. You, C. Saggese, Y. Li, H. Jung, L. Deng, I. Wlokas, H. Wang, Mobility size and mass of nascent soot particles in a benchmark premixed ethylene flame, Combust. Flame 162 (10) (2015) 3810–3822, doi:10.1016/j.combustflame.2015.07.018.

[2] C. Gu, H. Lin, J. Camacho, B. Lin, C. Shao, R. Li, H. Gu, B. Guan, Z. Huang, H. Wang, Particle size distribution of nascent soot in lightly and heavily soot-ing premixed ethylene flames, Combust. Flame 165 (2016) 177–187, doi:10.1016/j.combustflame.2015.12.002.

[3] L. Sgro, A. Barone, M. Commodo, A. D'Alessio, A. De Filippo, G. Lanzuolo, P. Minutolo, A. D'Alessio, A. De Filippo, G. Lanzuolo, P. Minutolo, Measurement of nanoparticles of organic carbon in non-sooting flame conditions, Proc. Combust. Inst. 32 I (1) (2009) 689–696, doi:10.1016/j.proci.2008.06.216.

[4] H. Bladh, N.E. Olofsson, T. Mouton, J. Simonsson, X. Mercier, A. Faccinetto, P.E. Bengtsson, P. Desgroux, Probing the smallest soot particles in low-sooting premixed flames using laser-induced incandescence, Proc. Combust. Inst. 35 (2) (2015) 1843–1850, doi:10.1016/j.proci.2014.06.001.

[5] J. Hwang, S. Chung, Growth of soot particles in counterflow diffusion flames of ethylene, Combust. Flame 125 (1–2) (2001) 752–762, doi:10.1016/S0010-2180(00)00234-0.

[6] R. Puri, T. Richardson, R. Santoro, R. Dobbins, Aerosol dynamic processes of soot aggregates in a laminar ethene diffusion flame, Combust. Flame 92 (3) (1993) 320–333, doi:10.1016/0010-2180(93)90043-3.

[7] H. Guo, Z. Gub, K.A. Thomson, G.J. Smallwood, F.F. Baksh, Soot formation in a laminar ethylene/air diffusion flame at pressures from 1 to 8 atm, Proc. Combust. Inst. 34 (1) (2013) 1795–1802, doi:10.1016/j.proci.2012.07.006.

[8] V. Chernov, M.J. Thomson, S.B. Dworkin, N.A. Slavinskaya, U. Riedel, Soot formation with C1 and C2 fuels using an improved chemical mechanism for pah growth, Combust. Flame 161 (2) (2014) 592–601, doi:10.1016/j.combustflame.2013.09.017.

[9] K.O. Johansson, M.P. Head-Gordon, P.E. Schrader, K.R. Wilson, H.A. Michelsen, Resonance-stabilized hydrocarbon-radical chain reactions may explain soot inception and growth, Science 361 (6406) (2018) 997–1000, doi:10.1126/science.aat3417.

[10] M. Thomson, T. Mitra, A radical approach to soot formation, Science 361 (6406) (2018) 978–979, doi:10.1126/science.aau5941.

[11] W. Yuan, Y. Li, F. Qi, Challenges and perspectives of combustion chemistry research, Science China Chem. 60 (11) (2017) 1391–1401, doi:10.1007/s11426-017-9066-9.

[12] J. Yang, L. Zhao, W. Yuan, F. Qi, Y. Li, Experimental and kinetic modeling investigation on laminar premixed benzene flames with various equivalence ratios, Proc. Combust. Inst. 35 (1) (2015) 855–862, doi:10.1016/j.proci.2014.05.085.

[13] N. Hansen, T. Kasper, S.J. Klippenstein, P.R. Westmoreland, M.E. Law, C.A. Taatjes, K. Kohse-Höinghaus, J. Wang, T.A. Cool, Initial steps of aromatic ring formation in a laminar premixed fuel-rich cyclopentene flame, J. Phys. Chem. A 111 (19) (2007) 4081–4092, doi:10.1021/jp0683317.

[14] T. Bierkandt, T. Kasper, E. Akyildiz, A. Lucassen, P. Oßwald, M. Köhler, P. Hemberger, Flame structure of a low-pressure laminar premixed and lightly sooting acetylene flame and the effect of ethanol addition, Proc. Combust. Inst. 35 (1) (2015) 803–811, doi:10.1016/j.proci.2014.05.094.

[15] L. Ruwe, K. Moshammer, N. Hansen, K. Kohse-Hinghaus, Consumption and hydrocarbon growth processes in a 2-methyl-2-butene flame, Combust. Flame 175 (2017) 34–46, doi:10.1016/j.combustflame.2016.06.032. Special Issue in Honor of Norbert Peters.

[16] N. Hansen, X. He, R. Griggs, K. Moshammer, Knowledge generation through data research: new validation targets for the refinement of kinetic mechanisms, Proc. Combust. Inst. (2018), doi:10.1016/j.proci.2018.07.023.

[17] M.J. Castaldi, N.M. Marinov, C.F. Melius, J. Huang, S.M. Senkan, W.J. Pit, C.K. Westbrook, Experimental and modeling investigation of aromatic and polycyclic aromatic hydrocarbon formation in a premixed ethylene flame, Symp. (Int.) Combust. 26 (1) (1996) 693–702, doi:10.1016/S0082-0784(96)80277-3.

[18] J. Huang, S.M. Senkan, Polycyclic aromatic hydrocarbon and soot formation in premixed flames of CH3Cl/CH4 and CH4, Symp. (Int.) Combust. 26 (2) (1996) 2335–2341, doi:10.1016/S0082-0784(96)80062-2.

[19] A. Mze Ahmed, S. Mancarella, P. Desgroux, L. Gasnot, J.F. Pauwels, A. El Bakali, Experimental and numerical study on rich methane/hydrogen/air laminar premixed flames at atmospheric pressure: Effect of hydrogen addition to fuel on soot gaseous precursors, Int. J. Hydrogen Energy 41 (16) (2016) 6929–6942, doi:10.1016/j.ijhydene.2015.11.148.

[20] T.R. Melton, A.M. Vincitore, S.M. Senkan, The effects of equivalence ratio on the formation of polycyclic aromatic hydrocarbons and soot in premixed methane flames, Symp. (Int.) Combust. 27 (2) (1998) 1631–1637, doi:10.1016/S0082-0784(98)80001-5.

[21] T.R. Melton, F. Inal, S.M. Senkan, The effects of equivalence ratio on the formation of polycyclic aromatic hydrocarbons and soot in premixed ethane flames, Combust. Flame 121 (4) (2000) 671–678, doi:10.1016/S0010-2180(99)00180-7.

[22] Internation sooting flame (ISF workshop), http://www.adelaide.edu.au/cet/isfworkshop/data-sets/laminar/.

[23] F. Carbone, K. Gleason, A. Gomez, Probing gas-to-particle transition in a moderately sooting atmospheric pressure ethylene/air laminar premixed flame. Part I: gas phase and soot ensemble characterization, Combust. Flame 181 (2017) 315–328, doi:10.1016/j.combustflame.2017.01.029.

[24] M. Bönig, C. Feldermann, H. Jander, B. Lüers, G. Rudolph, H. Wagner, Soot formation in premixed C2H4 flat flames at elevated pressure, Symp. (Int.) Combust. 23 (1) (1991) 1581–1587, doi:10.1016/S0082-0784(06)80429-7.

[25] H. Böhm, D. Hesse, H. Jander, B. Lüers, J. Pietscher, H. Wagner, M. Weiss, The influence of pressure and temperature on soot formation in premixed flames, Symp. (Int.) Combust. 22 (1) (1989) 403–411, doi:10.1016/S0082-0784(89)80047-5.

[26] F. Xu, P.B. Sunderland, G.M. Faeth, Soot formation in laminar premixed ethylene/air flames at atmospheric pressure, Combust. Flame 108 (1997) 471–493, doi:10.1016/S0010-2180(96)00200-3.

[27] Y. Xuan, G. Blanquart, Two-dimensional flow effects on soot formation in laminar premixed flames, Combust. Flame 166 (2016) 113–124, doi:10.1016/j.combustflame.2016.01.007.

[28] W.K. Metcalfe, S.M. Burke, S.S. Ahmed, H.J. Curran, A hierarchical and comparative kinetic modeling study of C1-C2 hydrocarbon and oxygenated fuels, Int. J. Chem. Kinet. 45 (10) (2013) 638–675, doi:10.1002/kin.20802.

[29] S.M. Burke, U. Burke, R. Mc Donagh, O. Mathieu, I. Osorio, C. Keesee, A. Morones, E.L. Petersen, W. Wang, T.A. DeVerter, M.A. Oehlschlaeger, B. Rhodes, R.K. Hanson, D.F. Davidson, B.W. Weber, C.J. Sung, J. Santner, Y. Ju, F.M. Haas, F.L. Dryer, E.N. Volkov, E.J. Nilsson, A.A. Konnov, M. Alrefae, F. Khaled, A. Farooq, P. Dirrenberger, P.A. Glaude, F. Battin-Leclerc, H.J. Curran, An experimental and modeling study of propene oxidation. Part 2: ignition delay time and flame speed measurements, Combust. Flame 162 (2) (2015) 296–314, doi:10.1016/j.combustflame.2014.07.032.

[30] E. Ranzi, A. Frassoldati, R. Grana, A. Cuoci, T. Faravelli, A. Kelley, C. Law, Hierarchical and comparative kinetic modeling of laminar flame speeds of hydrocarbon and oxygenated fuels, Prog. Energy Combust. Sci. 38 (4) (2012) 468–501, doi:10.1016/j.pecs.2012.03.004.

[31] B. Ruscic, Active thermochemical tables: sequential bond dissociation enthalpies of methane, ethane, and methanol and the related thermochemistry, J. Phys. Chem. A 119 (28) (2015) 7810–7837, doi:10.1021/acs.jpca.5b01346.

[32] E. Goos, A. Burcat, B. Ruscic, BurcatThermo, 2016, http://garfield.chem.elte.hu/Burcat/burcat.html.
[33] S.W. Benson, Thermochemical kinetics, 2nd ed., John Wiley & Sons, New York, 1976.
[34] N. Cohen, S.W. Benson, Estimation of heats of formation of organic compounds by additivity methods, Chem. Rev. 93 (7) (1993) 2419–2438, doi:10.1021/cr00023a005.
[35] T.S. Totton, A.J. Misquitta, M. Kraft, A quantitative study of the clustering of polycyclic aromatic hydrocarbons at high temperatures., Phys. Chem. Chem. Phys. 14 (12) (2012) 4081–4094, doi:10.1039/c2cp23008a.
[36] S.H. Chung, A. Violi, Peri-condensed aromatics with aliphatic chains as key intermediates for the nucleation of aromatic hydrocarbons, Proc. Combust. Inst. 33 (1) (2011) 693–700, doi:10.1016/j.proci.2010.06.038.
[37] W. Pejpichestakul, A. Frassoldati, A. Parente, T. Faravelli, Kinetic modeling of soot formation in premixed burner-stabilized stagnation ethylene flames at heavily sooting condition, Fuel 234 (July) (2018) 199–206, doi:10.1016/j.fuel.2018.07.022.
[38] C. Saggese, S. Ferrario, J. Camacho, A. Cuoci, A. Frassoldati, E. Ranzi, H. Wang, T. Faravelli, Kinetic modeling of particle size distribution of soot in a premixed burner-stabilized stagnation ethylene flame, Combust. Flame 162 (9) (2015) 3356–3369, doi:10.1016/j.combustflame.2015.06.002.
[39] W. Pejpichestakul, E. Ranzi, M. Pelucchi, A. Frassoldati, A. Cuoci, A. Parente, T. Faravelli, Examination of a soot model in premixed laminar flames at fuel-rich conditions, Proc. Combust. Inst. 37 (2019) 1013–1021, doi:10.1016/j.proci.2018.06.104.
[40] A. Cuoci, A. Frassoldati, T. Faravelli, E. Ranzi, A computational tool for the detailed kinetic modeling of laminar flames: application to C2H4/CH4 coflow flames, Combust. Flame 160 (5) (2013) 870–886, doi:10.1016/j.combustflame.2013.01.011.
[41] A. Cuoci, A. Frassoldati, T. Faravelli, E. Ranzi, Opensmoke++: an object-oriented framework for the numerical modeling of reactive systems with detailed kinetic mechanisms, Comput. Phys. Commun. 192 (2015) 237–264, doi:10.1016/j.cpc.2015.02.014.
[42] W. Grosshandler, RADCAL: a narrow-band model for radiation calculations in a combustion environment, NIST Technical Note 1402, 1993.
[43] R.S. Barlow, A.N. Karpetis, J.H. Frank, J.Y. Chen, Scalar profiles and NO formation in laminar opposed-flow partially premixed methane/air flames, Combust. Flame 127 (3) (2001) 2102–2118, doi:10.1016/S0010-2180(01)00313-3.
[44] R.J. Kee, F.M. Rupley, E. Meeks, J.A. Miller, CHEMKIN-III: a Fortran chemical kinetics package for the analysis of gas phase chemical and plasma kinetics, Sandia National Laboratories Report, 1996.
[45] C. Saggese, A. Cuoci, A. Frassoldati, S. Ferrario, J. Camacho, H. Wang, T. Faravelli, Probe effects in soot sampling from a burner-stabilized stagnation flame, Combust. Flame 167 (2016) 184–197, doi:10.1016/j.combustflame.2016.02.013.
[46] A. Stagni, A. Cuoci, A. Frassoldati, E. Ranzi, T. Faravelli, Numerical investigation of soot formation from microgravity droplet combustion using heterogeneous chemistry, Combust. Flame 189 (2018) 393–406, doi:10.1016/j.combustflame.2017.10.029.
[47] W. Pejpichestakul, A. Frassoldati, A. Parente, T. Faravelli, Soot modeling of ethylene counterflow diffusion flames, Combust. Sci. Technol. (2018) in press, doi:10.1080/00102202.2018.1540472.
[48] C.-W. Zhou, Y. Li, U. Burke, C. Banyon, K.P. Somers, S. Ding, S. Khan, J.W. Hargis, T. Sikes, O. Mathieu, E.L. Petersen, M. AlAbbad, A. Farooq, Y. Pan, Y. Zhang, Z. Huang, J. Lopez, Z. Loparo, S.S. Vasu, H.J. Curran, An experimental and chemical kinetic modeling study of 1,3-butadiene combustion: ignition delay time and laminar flame speed measurements, Combust. Flame 197 (2018) 423–438, doi:10.1016/j.combustflame.2018.08.006.
[49] M.R. Djokic, K.M. Van Geem, C. Cavallotti, A. Frassoldati, E. Ranzi, G.B. Marin, An experimental and kinetic modeling study of cyclopentadiene pyrolysis: first growth of polycyclic aromatic hydrocarbons, Combust. Flame 161 (11) (2014) 2739–2751, doi:10.1016/j.combustflame.2014.04.013.
[50] A.M. Mebel, Y. Georgievskii, A.W. Jasper, S.J. Klippenstein, Temperature- and pressure-dependent rate coefficients for the HACA pathways from benzene to naphthalene, Proc. Combust. Inst. 36 (1) (2017) 919–926, doi:10.1016/j.proci.2016.07.013.
[51] M. Maricq, Size and charge of soot particles in rich premixed ethylene flames, Combust. Flame 137 (3) (2004) 340–350, doi:10.1016/j.combustflame.2004.01.013.
[52] A.D. Abid, J. Camacho, D. Sheen, H. Wang, Quantitative measurement of soot particle size distribution in premixed flames—the burner-stabilized stagnation flame approach, Combust. Flame 156 (10) (2009) 1862–1870, doi:10.1016/j.combustflame.2009.05.010.
[53] J. Appel, H. Bockhorn, M. Frenklach, Kinetic modeling of soot formation with detailed chemistry and physics: laminar premixed flames of C2 hydrocarbons, Combust. Flame 121 (1–2) (2000) 122–136, doi:10.1016/S0010-2180(99)00135-2.